

Cells exploit a phase transition to establish interconnections in fibrous extracellular matrices

Georgios Grekas^{1,2,*}, Maria Proestaki³, Phoebus Rosakis^{1,2,*}, Jacob Notbohm³, Charalambos Makridakis^{1,2,4}
& Guruswami Ravichandran⁵

¹*Department of Mathematics and Applied Mathematics, University of Crete, Greece,*

²*Institute of Applied & Computational Mathematics, Foundation for Research & Technology-Hellas, Heraklion, Greece,*

³*Department of Engineering Physics, University of Wisconsin-Madison, USA*

⁴*Department of Mathematics, MPS, University of Sussex, Brighton, United Kingdom*

⁵*Division of Engineering and Applied Science, California Institute of Technology*

By exerting mechanical forces, biological cells generate striking spatial patterns of localised deformation in the surrounding collagen network. Tethers—paths of high densification and fiber alignment—form between cells, and radial hair-like bands emanate from cell clusters. While tethers facilitate cell communication, the mechanism for their formation is unclear. Here we combine modelling, simulation and experiment, and explore unexpected similarities with martensitic microstructures in shape memory alloys; we show that tether formation is a densification phase transition of the fibrous extracellular matrix, caused by buckling instability of network fibers under cell-induced compression. Our model uses multiscale averaging over fiber orientations to obtain a two-phase, bistable continuum strain energy density for fibrous collagen, with a densified second phase. Simulations predict strain discontinuities

between the undensified and the densified phase, which localises within intercellular tethers and radial emanations from cell clusters, as experimentally observed. Ruling out biochemical factors, our experiments use contracting active hydrogel particles to produce similar—but controlled—localised deformations as contractile cells. Our results reveal subtle connections with martensitic phase transitions that demonstrate how, by exploiting a special instability, cells spontaneously generate pathways to each other in a 3D complex medium simply by contracting, with implications on intercellular mechanosensing and the remodelling of matrix mechanical properties by tether networks.

If the fibrous extracellular matrix (ECM) were a typical elastic material, deformations due to cells contracting would decay with distance within a few cellular diameters^{1,2}. Instead, the observations of Weiss³ and Harris & Stopak^{4,5} led the way^{6–9} in showing dramatic spatial patterns of densification and fiber alignment, localised within tether-like bands joining distant cell clusters (Fig. 1a), but also radial hair-like emanations from each cluster of cells (Fig. 1c). Tethers were recently observed between individual cells^{2,7} as well (Fig. 1b). Evidence is mounting that these patterns are important for intercellular communication and motility: individual cells leave their cluster and move along a tether to neighbouring clusters^{4,5,7,8}; single fibroblasts joined by a tether grow appendages along it toward each other². Cancer cells preferentially invade along densified regions of the ECM¹⁰.

Along the axis of each tether, the ECM is stretched by as much as 40%, but also compressed in the transverse direction to half or even a quarter of its original thickness^{8,9}. Density can be 3

to 5 times higher within tethers than without. These deformations are not only severe, but also spatially localised within tethers⁴, and along radial hairlike bands that issue from individual cell clusters⁵ (Fig. 1c). What is the mechanism underlying the formation of these patterns? Many studies focus on the behaviour of collagen in tension, and argue that alignment and densification are induced by tensile strain⁷, or are due to a stiffening nonlinearity of the stress-strain behaviour of the ECM in tension^{11,12}. At the same time, density within tethers exceeds the undeformed value by almost an order of magnitude^{8,9}; this implies compressive strains at least twice as large as tensile ones in magnitude (see Supplemental Information: Compressive Stretch Estimate). While cells, by contracting, apply radial tensile forces to the ECM they adhere to, they also decrease their perimeter, thereby inducing compression in the circumferential direction^{2,13}. The ECM ligament between two cells, where a tether forms, is thus under axial tension and transverse compression, but the observed compressive strains are unexpectedly large⁸. The degree of localisation of densification is also unexpected. Centimetre-scale tethers induced by multi-cell tissue explants have well defined boundaries, across which the density is virtually discontinuous^{4,5} (Fig. 1a). A large number of thinner radial bands issue from each explant. At scales comparable to fiber length, the density localisation is gradual but still quite pronounced², while fewer radial bands emerge from each cell (Fig. 1b). Solitary cell clusters also produce radial bands (Fig. 1c)^{4,5}. Deformations are therefore strongly inhomogeneous in the angular coordinates and radial symmetry is broken. What is surprising in these observations is the persistent appearance of localised, inhomogeneous deformations, not only at the scale of fiber network inhomogeneity, but at macroscopic scales as well. Current nonlinear continuum models do not explain these patterns of localisation^{9,12,13}.

Here we argue that these phenomena are due to a material instability which stems from a special nonlinearity in individual fiber behaviour and the inhomogeneity of the fibrous network. Clues as to the nature of this come from experiments in larger-scale networks (open-cell foams¹⁴) and fibrin¹⁵. Rather like rubber bands, individual fibers support tensile forces and may stiffen with increasing tension^{16,17}, but buckle under compression, losing stiffness and eventually collapsing. Larger polyhedral groups of fibers buckle and collapse under compression¹⁴. These buckling instabilities cause the appearance of bands of intense compressive deformation and high density, within which fibers are mostly buckled and compacted, alternating with bands of normal density and low compressive strain, where fibers are largely unbent and loosely arranged. These two region types (high- and low-density) are separated by sharp interfaces, across which strain and density jump discontinuously at the macroscopic scale. This behaviour is bistable, with coexistence of a densified phase and an undensified phase. The theory of mechanical diffusionless isothermal phase transitions has been used to model this in the one-dimensional context of uniaxial compression^{14,15}. Here we develop a higher dimensional model for general deformations.

Modelling the Energy Landscape of the Fibrous ECM

We model the nonlinear elastic energy landscape of the fibrous ECM, starting from the relation between force S and effective stretch $\lambda = d/l_0$ for a single flexible elastic fiber; here d is the distance between endpoints, l_0 is the relaxed (reference) length. See Methods and Supplemental Fig. S1a for details. We assume $S(\lambda)$ stiffens in tension (its slope increases with $\lambda > 1$) as is common for biopolymers^{16–18}. Aside from direct observation of buckling^{19–21}, very little is known

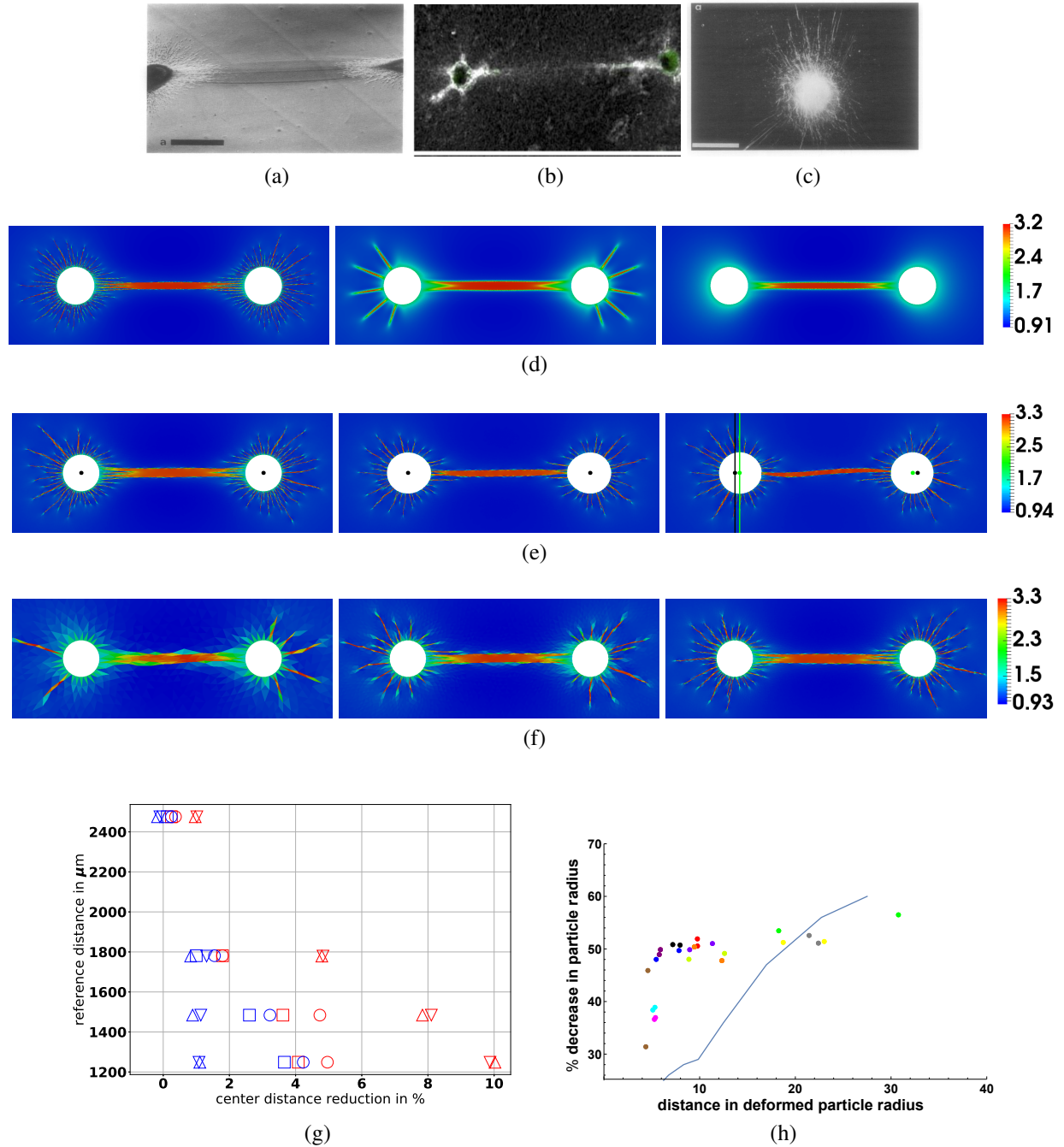


Figure 1: Tethers joining Hairy Clusters: A tether between (a) mm sized explants (reproduced from⁵) and (b) μm -sized individual cells (reproduced from²). (c) Radial hairs issuing from an explant (reproduced from⁵). (d) Smoothing effect of higher gradient energy. (I) $\varepsilon = 0$, (II) $\varepsilon = 0.01R$, (III) $\varepsilon = 0.05R$, where R is particle radius. (e) Shape of deformable explants and relative motion (I) $k = \infty$ with fixed centres. (II), $k = 1$ with fixed centres. (III), $k = 1$ but centres are free, and move from black to green dot. (f) Fineness of phase mixture in numerical solutions depends on mesh resolution (increasing from left to right). (g) Relative motion of centres of four pairs of active particles joined by a tether in contraction (red) - expansion (blue) cycles. Triangles: simulation results. Squares/circles: experiments. (h) Predicting whether a tether forms between two particles. Blue curve: separatrix constructed from simulations. Axes: % decrease in particle radius versus deformed distance (in deformed particle radii). Above separatrix, tethers are predicted to form between particle pairs (same colour). No tether is predicted to form below separatrix. Our experimental data (each pair is one colour) abide by the prediction. Scalebar: ratio of deformed to undeformed density.

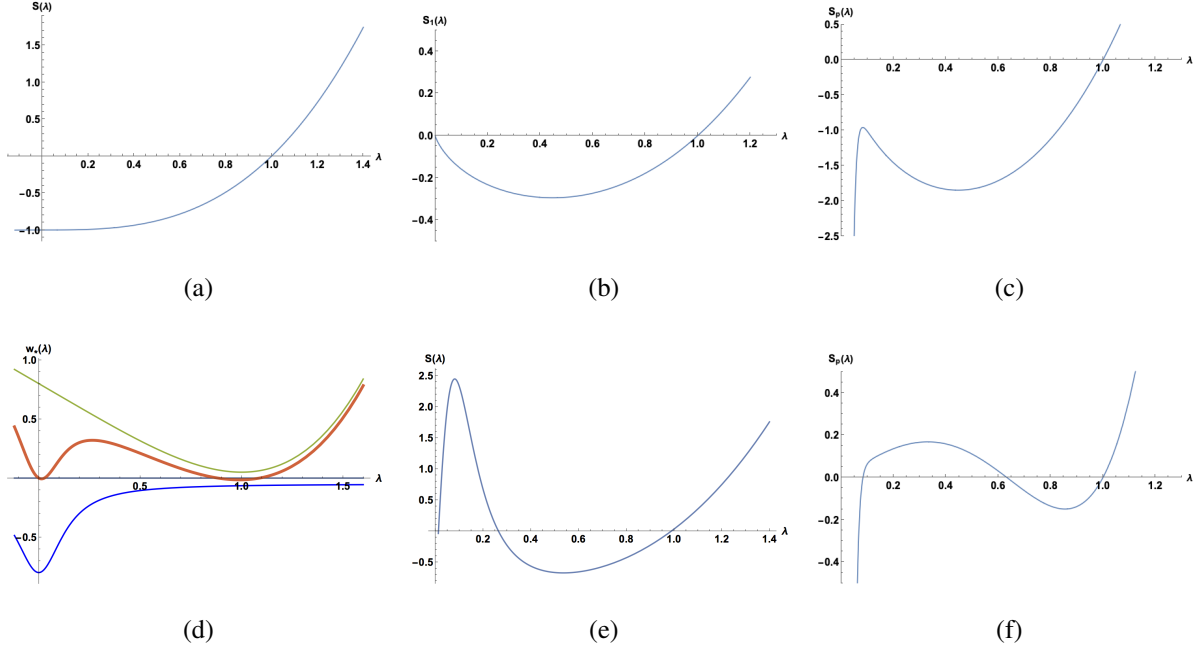


Figure 2: One Well or Two? Designing an Energy Density for Fibrous ECM: (a) Force-stretch curve of a single fiber that loses stiffness in compression and stiffens in tension. (b) Uniaxial compression stress-stretch curve of orientation-averaged energy density corresponding to (a) has a decreasing unstable branch. (c) As in (b) but with energy penalty due to fiber volume added, which resists extreme compression. (d) Adding an attraction potential (blue) to the fiber potential (green) corresponding to (a) produces a two-well bistable potential (red). (e) Force-stretch curve corresponding to the red potential in (d). (f) Uniaxial compression curve of the corresponding orientation-averaged energy density (with volume penalty) has two stable stress-free states (bistability), and an unstable one in the middle.

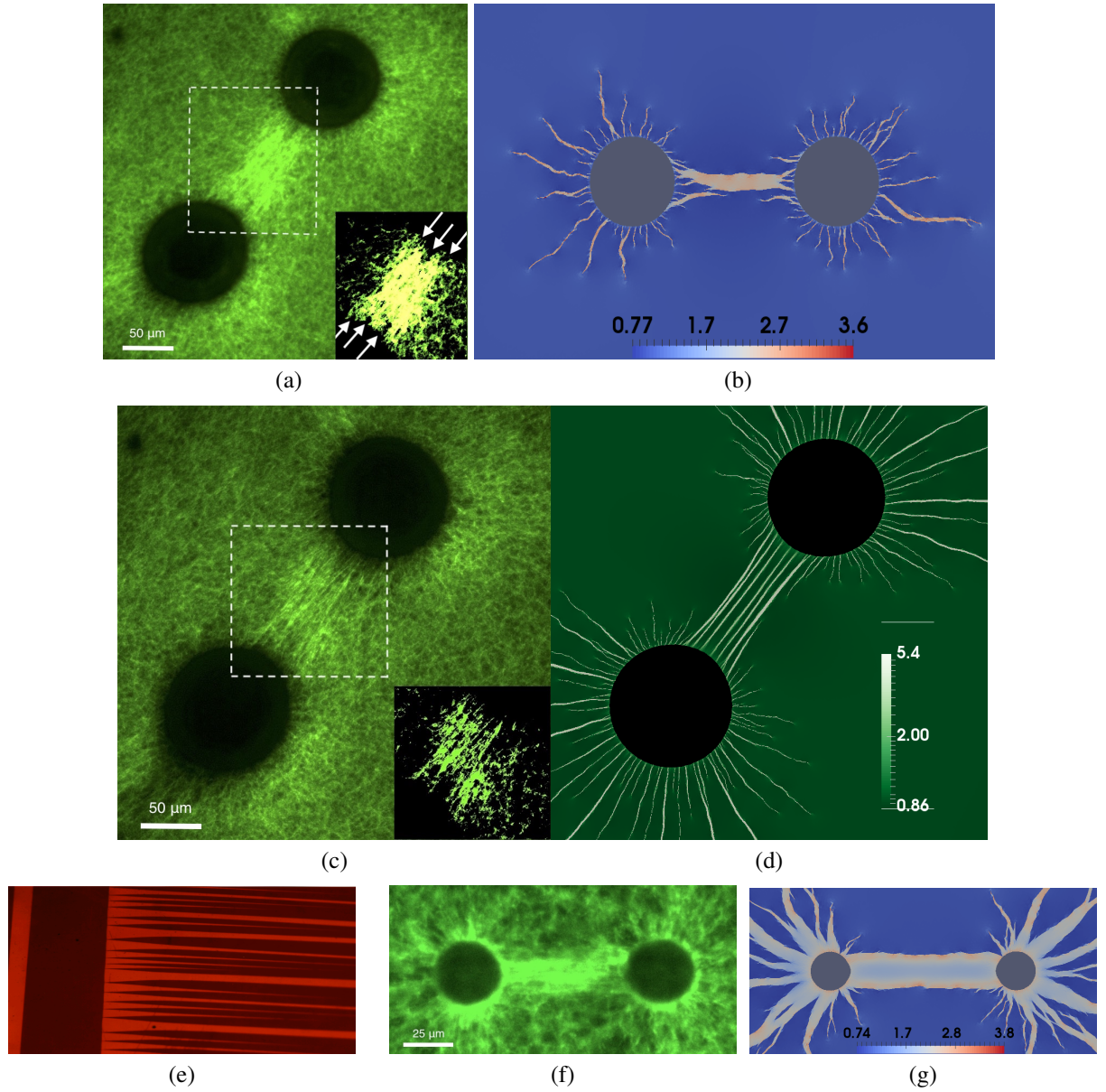


Figure 3: Splitting Hairs, Twins and Tethers: (a) and (b) experiment and qualitative simulation of a particle pair with low contraction $< 45\%$. Insert shows high-contrast version of area within dotted rectangle. Note partial tether splitting near particle boundary. Arrows point at locations where tether splits near particle boundary. Note radial hairs also splitting in (b). (c) A tether fully split into multiple thin bands. Insert shows high-contrast version of area within dotted rectangle. (d) Simulation with initial radii, distances and contractions matched with (c). (e) martensitic twins (courtesy of C. Chu & R.D. James) split into multiple bands; some bands have split tips near incompatible vertical boundary. (f) Two smaller particles with full-contact tether (except torn fibers at right particle), and partially enveloping densification. (g) qualitative simulation of (f). Scalebar: ratio of deformed to undeformed density.

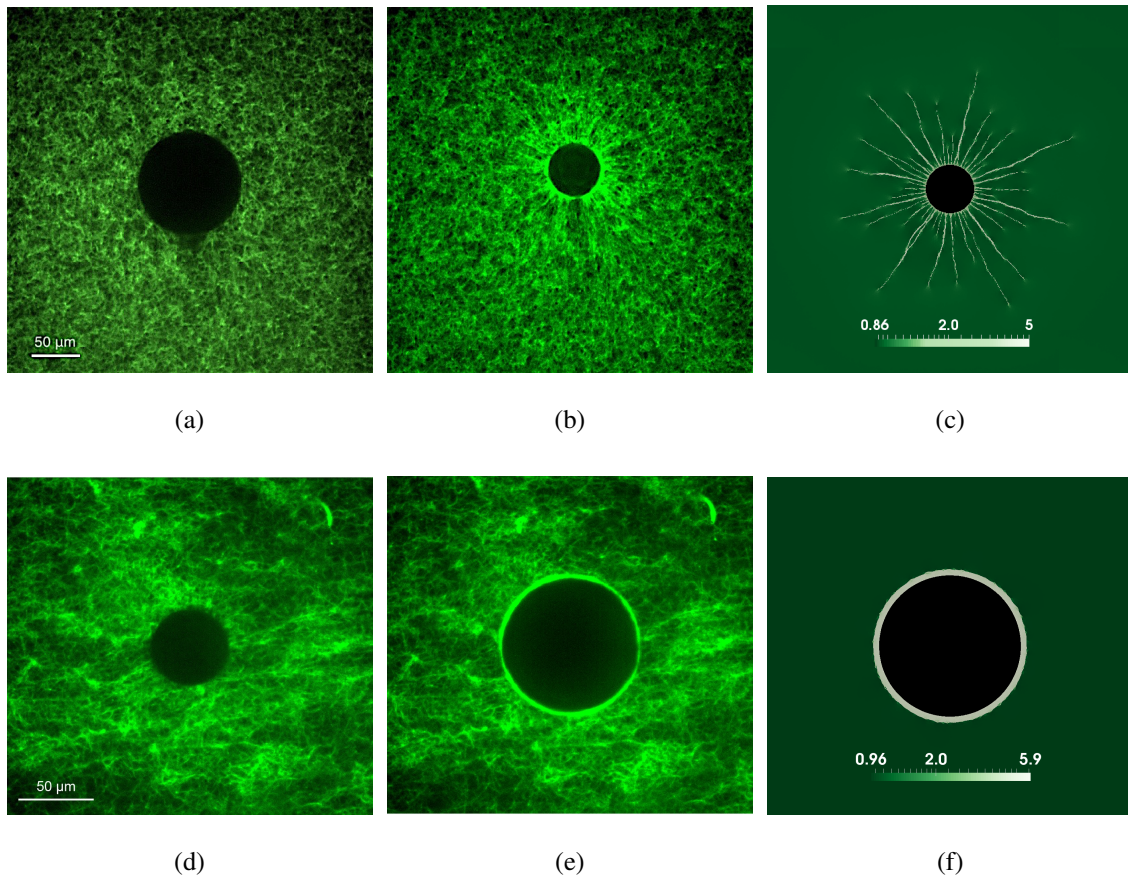


Figure 4: Contracting vs Expanding Particle: Experiments and Simulations. (a)-(c) Contracting particle. (a) Undeformed PNIPAAm particle. (b) PNIPAAm particle radially contracted by 50% (c) Simulation of contracting particle. Note radial “hairs” and radial symmetry breaking. (d)-(f) Expanding particle. (d) Unexpanded (undeformed) PNIPAAm particle (e) PNIPAAm particle radially expanded by 50%. Note circumferential bright densification layer. (f) Simulation prediction for radially expanded particle. Note radially symmetric densified phase layer surrounding particle and circumferential phase boundary. Scalebar: ratio of deformed to undeformed density.

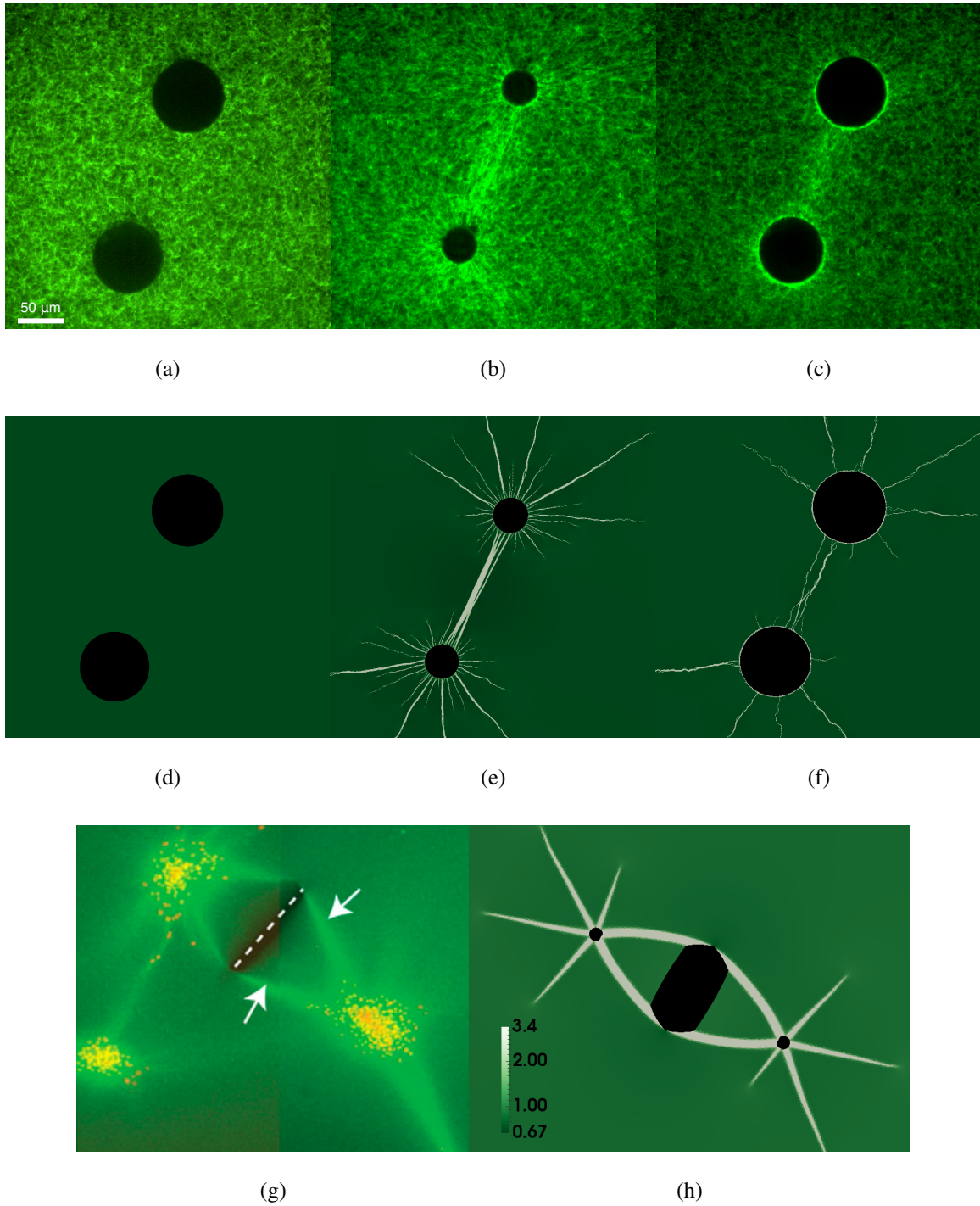


Figure 5: Reversing Contraction and Cutting Tethers: (a) two uncontracted active particles at 26°C (b) Contracted at 39°C (c) re-expanded at 26°C. (d)-(f) simulations of (a)-(c) with matched initial radii, distance between centres and contractile strains. Note densification ring-around-the-particle in (c) and (f). (g)-(h) A crack (dotted line) is cut across a tether between acini⁸, the tether disappears. (g) Two new tethers turn around the corners of the crack to bypass it (reproduced from⁸). (h) Simulation of pair of acini with crack predicts bypassing the crack. Scalebar: ratio of deformed to undeformed density.

about the post-buckling behaviour of individual collagen or fibrin fibers in compression²², as λ decreases from 1 toward 0 (total collapse). This depends on their bending behaviour, which is difficult to characterise, because of their inhomogeneous, hierarchical structure¹⁸ as bundles of loosely connected fibrils. We choose $S(\lambda)$ as in Fig. 2a so that there is stiffening in tension ($\lambda > 1$) but loss of stiffness in compression ($\lambda < 1$) because of buckling. An example is $S(\lambda) = \mu(\lambda^3 - 1)$ (Fig. 2a). The corresponding elastic energy of the fiber is then $w(\lambda) = \int_1^\lambda S(\lambda') d\lambda'$. Suppose the undeformed 2D network has a uniform distribution of fiber orientations. When subjected to a 2D deformation, the deformed stretch ratio of a fiber making an angle θ with the principal axes of stretch in the reference configuration is $\sqrt{(\lambda_1 \cos \theta)^2 + (\lambda_2 \sin \theta)^2}$, where λ_1, λ_2 are the principal stretches of the deformation (see Methods). Summing over all orientation angles, we find the elastic energy density of the network, following Treloar's approach²³ and the virtual internal bond model^{24, 25}:

$$\hat{W}(\lambda_1, \lambda_2) = \frac{1}{2\pi} \int_0^{2\pi} w \left(\sqrt{(\lambda_1 \cos \theta)^2 + (\lambda_2 \sin \theta)^2} \right) d\theta, \quad (1)$$

see Methods for more details and an explicit form of this energy. Surprisingly, this energy density has a stress-strain relation in uniaxial compression $S_1(\lambda) = \partial \bar{W}(\lambda, 1) / \partial \lambda$ (Fig. 2b) that is not monotonic, but its slope becomes negative for λ below a critical value. This is unexpected, since the original single fiber stress $S(\lambda)$ is monotone increasing. Nonetheless, with increasing compression as λ decreases toward 0, the network loses stiffness because of buckling of more fibers. Also, fibers reorient due to compression, increasing the angle they make with the compression axis, so they support less load along the compression axis (see Supplemental Information: Stiffness Loss). As a result, the stiffness eventually becomes negative (strain softening), triggering a compression

instability.

Physically, we expect that increasing compression ($\lambda \rightarrow 0$) leads to densification, and fibers getting squeezed together, thereby resisting further compression, eventually restoring stability. To account for fiber volume, we add a fiber volume penalty term (Eq. (9) and Supplemental Fig. S1b) to the energy²⁵ (1), which will resist collapse in the crushing limit as the volume ratio $J = \lambda_1 \lambda_2 \rightarrow 0$,

$$W(\mathbf{F}) = \bar{W}(\lambda_1, \lambda_2) = \hat{W}(\lambda_1, \lambda_2) + \exp[A(b - \lambda_1 \lambda_2)]$$

with A a large and b a small positive constant (here \mathbf{F} is the deformation gradient). As expected, this restores positive stiffness at extreme compressions (Fig. 2c). Thus there is an unstable regime (decreasing branch in the S_1 vs λ curve in Fig. 2c) separating two stable phases (increasing branches); a low compression phase and a densified phase. This allows banding deformations with alternating zones of low and high densification, separated by sharp interfaces normal to the compression axis, as observed in open-cell foams and fibrin^{14,15}. The two phases coexist under the same compressive stress. This bistable behaviour has much in common with that of shape-memory materials²⁶.

In this model, the densified phase is only stable under compressive stress; this is appropriate for crosslinked networks⁷. In uncrosslinked networks, after compression is removed, part of the densified phase remains in the ECM^{7,9,19,27,28}. Various factors may contribute to this, such as adhesion and crosslinking of fibers that come into contact due to densification, subject to van der Waals, or other noncovalent types of attraction²⁷. We model this by adding a short range adhesion potential $w_a(\lambda)$ (blue curve in Fig. 2d) to the single fiber buckling potential $w(\lambda)$ (green curve in

Fig. 2d). This renders fiber collapse energetically favourable at short distances of the endpoints (λ near zero). The resulting single fiber potential $w_*(\lambda) = w(\lambda) + w_a(\lambda)$ is now a two-well potential (red curve in Fig. 2d) with a new minimum corresponding to a collapsed fiber state ($\lambda = 0$) that is stable under zero load. Replacing $w(\lambda)$ by $w_*(\lambda)$ in (1) we obtain a bistable energy $W_*(\mathbf{F})$ that has multiple global minima (Supplemental Fig. S2a) compared to the single minimum of the monostable energy $W(\mathbf{F})$ (Supplemental Fig. S2b) . See Supplemental Information: Individual Fiber Behaviour, for additional reasons in favour of a two well potential.

What sets both energy densities W and W_* apart from previous nonlinear elastic models of fibrous ECM^{12,13} is instability, which they share with certain non-convex nonlinear elastic models^{29–32}. These models were developed for austenite-martensite phase transformations, twinning, and the shape memory effect. The essential common features are as follows: (i) Both W and W_* suffer a loss of stability; a property known as strong ellipticity^{29,33,34} fails at some strains, whereby some higher dimensional measure of stiffness becomes negative³⁵. See Supplemental Information: Ellipticity Loss and Supplemental Fig. S2d, S2e. Avoiding these unstable states leads to equilibrium deformations with discontinuous strains²⁹. (ii) The bistable energy density W_* is a multi-well potential (Supplemental Fig. S2a) . Although the monostable energy density W has a single minimum (Supplemental Fig. S2b) , the associated Gibbs free energy $W(\mathbf{F}) - \mathbf{S} \cdot \mathbf{F}$ is a double well potential for some values of the stress \mathbf{S} , with minima close to those of W_* (Supplemental Fig. S2c) . This means that under suitable stress the monostable energy exhibits bistable behaviour as well. (iii) The energy minima satisfy geometric compatibility conditions³⁰ allowing the two corresponding strain states to occur simultaneously in the material, separated by a coher-

ent phase boundary³¹ (see Supplemental Information: Compatibility). The energy minimal strains correspond to principal stretches $(\lambda_1, \lambda_2) = (1, 1)$ (undeformed state) and $(\lambda_1^*, \lambda_2^*) = (0.2, 1.06)$, which is a severe uniaxial compression with strain $\varepsilon_1 = \lambda_1^* - 1 = -0.8$, combined with a moderate extension in the perpendicular direction $\varepsilon_2 = \lambda_2^* - 1 = 0.06$. These two energy wells correspond to the undensified phase and the densified phase of the material, respectively. An additional minimum at $(\lambda_1, \lambda_2) = (0.45, 0.45)$ is not compatible with the undeformed state $(1, 1)$ (see Supplemental Information: Compatibility). This explains why it is never encountered in our simulations.

The elastic energy of the ECM undergoing a deformation $\mathbf{y}(\mathbf{x})$ is

$$E\{\mathbf{y}\} = \int_{\Omega} W(\nabla \mathbf{y}(\mathbf{x})) d\mathbf{x} \quad (2)$$

where Ω is the undeformed region occupied by the ECM. Going from the discrete energy of a random fiber network of characteristic fiber size ε to the continuum energy in an asymptotic expansion^{24,36} as $\varepsilon \rightarrow 0$, one obtains (2) as the first term, followed by a higher gradient term quadratic in $\varepsilon \nabla \nabla \mathbf{y}(\mathbf{x})$. Here we choose a simple form of an isotropic higher gradient energy^{37,38}

$$G_{\varepsilon}\{\mathbf{y}\} = \frac{\varepsilon^2}{2} \int_{\Omega} |\nabla \nabla \mathbf{y}(\mathbf{x})|^2 d\mathbf{x} \quad (3)$$

To model contractile cells and multi-cell clusters (explants^{4,5}, acini^{8,9}), we let Ω contain initially circular cavities. At the boundary of each cavity, forces can be exerted onto the ECM. Each cell or cluster is represented by a collection of linear springs connecting each cavity boundary point to a central point which is allowed to move (Supplemental Fig. S1c). This contributes to the energy a term

$$C\{\mathbf{y}; \mathbf{z}_1, \dots, \mathbf{z}_n\} = \sum_{i=1}^n \int_{\Gamma_i} \frac{k}{2} \left[|\mathbf{y}(\mathbf{x}) - \mathbf{z}_i| - (R - u_0) \right]^2 ds_{\mathbf{x}} \quad (4)$$

where Γ_i is the boundary of the i^{th} cavity ($i = 1, \dots, n$), k is the spring stiffness, \mathbf{z}_i the variable centre position of the i^{th} cell, R the undeformed radius, and u_0 the cellular spring contraction. In contrast to previous studies^{2,9} cells or clusters need not remain circular after deformation and their centres can move. The smaller the value of k the larger the deviation of deformed cluster shape from circularity. For stiffer active particles we employ a slight modification (see Methods: Model for Active Particles and Supplemental Fig. S1d).

The total energy to be minimised is the sum of (2), (3) and (4):

$$\Phi\{\mathbf{y}; \mathbf{z}_1, \dots, \mathbf{z}_n\} = E\{\mathbf{y}\} + G_\varepsilon\{\mathbf{y}\} + C\{\mathbf{y}; \mathbf{z}_1, \dots, \mathbf{z}_n\} \quad (5)$$

Experiments and Simulations of ECM Deformations Induced by Active Particles

To ascertain that the densification and strain localised in tethers and radial bands is due solely to mechanical forces, and not to other biochemical factors, we embedded active hydrogel microspheres²¹ into Collagen I instead of cells. These PNIPAAm particles undergo a temperature-induced phase transition, causing their radius to contract by as much as 60% when heated above 32°C. Advantages of this are that we can control the amount of contraction via temperature, and even cause reverse re-expansion by cooling, without recourse to chemical means. See Methods for more details.

After developing a suitable finite element scheme that can handle deformation gradient discontinuities (details in Methods) we minimise the total energy (5) with respect to the deformation field $\mathbf{y}(\mathbf{x})$ and the cell centre positions \mathbf{z}_i . The simulated ECM domain contains one or more initially circular cavities of radius R , representing a cell or cell cluster, or an active contracting

particles used in our experiments. Choosing $u_0 > 0$ in (4) causes contraction of the natural length of the springs comprising the cell model from R to $R - u_0$, thus exerting centripetal forces onto the cavity boundaries.

The most striking features of our numerical solutions involving two contracting cavities are the tether^{4,5,8,9}, a zone of high density joining the two clusters, and thinner hairlike bands emerging from each cluster in the radial direction^{4,5}, tapering off and terminating within the domain (Fig. 1) Within each tether and radial band, the stretches are in the densified phase; outside they take values in the undensified phase. Density is discontinuous across the boundary of tethers and radial bands, and the ratio of densities outside and inside the tether is in the range 3-5. Within each tether there is tension along the tether axis and compression in the transverse direction. The compressive stretch is discontinuous across the tether boundary and as low as 30% (compressive strain is as high as 70%); the tensile stretch is much smoother although it is higher within tethers, with tensile strains as high as 140%. This contrast is observed in experiments⁹, it happens because the energy bistability occurs in compression. For a discontinuous strain, compatibility (displacement continuity across a phase boundary) allows the stretch normal to the tether boundary to jump, but the transverse one to be continuous, as observed⁹ and found in our simulations (Supplemental Fig. S3)

We depart from common practice^{2,9} and allow cells and clusters to change shape and move during ECM deformation in our model. Isolated explants^{4,5} remain circular after contraction; neighbouring clusters connected by a tether lose circularity^{4,5} and become egg-shaped with pointed ends toward each other (Fig. 1e) due to tether tension. Contracting active particles in our exper-

iments and simulations move towards each other by as much as 6% of their original distance (Fig. 1g), while remaining nearly spherical. For low values of cellular spring stiffness k in (4), shape changes are more pronounced, especially when cell centres are fixed, and to a lesser extent for free centres (Fig. 1e). This may explain why in experiments, the largest shape changes^{4,5} (Fig. 1a) occur in thin films on substrates which may constrain cluster motion, whereas in bulk ECM, shape changes are less pronounced and particles centres approach each other.

How close do two active particles have to be, and how much must they contract to form a tether between them? Multiple simulations provided a curve of particle radial strain versus distance, above which a tether forms joining particles, and below which none forms. Data from our experiments agreed with this prediction (Fig. 1h).

In our experiments, tethers between active particles branch off into multiple tips at points of contact with particles (Fig. 3a,3b), or even separate completely into thinner parallel bands (Fig. 3c, 3d). In contrast, tethers between contractile acini observed in⁷⁻⁹ are shaped like uniform strips that make full contact with each acinus, as in Fig. 3g. A layer of the densified phase envelopes each acinus before splitting into radial strands further out; see Fig. 5g. Why this disparity? Unexpectedly the answer lies in austenite-martensite transformations, where the Bain strain at the martensitic energy minimum³⁹ is incompatible with zero-strain austenite^{30,31} (see Supplemental Information: Compatibility). This means that these two minimum-energy strains cannot occur on either side of a phase boundary (strain discontinuity) without causing a mismatch in displacements. This forces splitting and tapering of twin bands in a crystal near an incompatible boundary⁴⁰ (Fig. 3e). Here as

well, energy minimisation compels strains not to stray far from energy density minima. In case of stiff active particles, the azimuthal stretch $\lambda_0 = 1 - u_0/R \approx 0.65$ imposed at the particle boundary by contraction is incompatible with the stretch $\lambda_1^* = 0.2$ corresponding to the densified phase energy well. To avoid this mismatch while maintaining displacement continuity, tethers must split and taper into points where they meet the particle boundary (Fig. 3a, 3c). Simulations confirm that when the imposed particle stretch λ_0 is closer to 1 (undensified phase) than to λ_1^* , tethers tend to split in the vicinity of the particle boundary (Fig. 3b) or even all along their axis (Fig. 3d). However, for $\lambda_0 \approx \lambda_1^*$ the densified phase is in full contact and envelopes the particle because of enhanced compatibility (Fig. 3g), as observed for a pair of smaller active particles (Fig. 3f) that contracted more than large ones (Fig. 3a). Acini⁷⁻⁹ and single cells² (Fig. 1b) can contract much more than active particles (up to 80% radius reduction^{8,9}) which corresponds to an azimuthal stretch close to λ_1^* . Compatibility allows tethers like uniform strips in full contact with each acinus, as in Fig. 3g.

What causes the densified phase to split into thin radial bands around particles? (Fig. 1c^{4,5}, Fig. 1f). A contracting inclusion induces radial tension and circumferential compression. Since the energy is bistable in compression, phase change tends to occur along the direction of compression, with phase boundaries normal to it, roughly along radial lines (Fig. 4b). Instead, an expanding particle would create radial compression, hence a circumferential phase boundary and densified layer (Fig. 4e). The stark contrast between the ECM's response to contracting and expanding particles is seen in our experiments (Fig. 4) and—possibly for the first time—captured by a continuum model. (Fig. 4c, 4f; also re-expanded particle in Fig. 5c, 5f).

For contracting particles, the radial orientation of interfaces forces finer splitting of the densified phase into narrower bands, as with tethers, in order to lower the cost of matching displacements at the particle boundary, while approaching the undensified state far away. These spatially fine phase mixtures establish a further connection with the nonlinear elastic theory of phase transitions^{30,31} in crystals. In some minimisation problems with a multi-well energy for austenite-martensite mixtures, it is known that the material cannot reach a global energy minimum^{30,41} because of strain incompatibility. Instead it tries to decrease energy by refinement: increasing the number of strain discontinuities and bands in alternating phases, while decreasing their size. This causes observed finely twinned martensitic microstructures⁴². In computations^{43,44} this phenomenon manifests itself as an increase in the number and spatial frequency of twin boundaries with increasing numerical mesh resolution. Similarly, when we decrease mesh size in our simulations, the number of radial bands issuing from each cluster increases and their thickness decreases (Fig. 1f).

In order to show that this mesh dependence is not a numerical artefact, we add the higher gradient term (3) to the energy. This introduces a length scale proportional to ε , which is an additional material parameter related to characteristic fiber length, bending stiffness and other parameters of the fiber network²⁴. For larger values of ε there are fewer, thicker radial bands, above a critical value, they disappear, while the tether persists (Fig. 1d). The presence of this term has a smoothening effect as it penalises high strain gradients; strain discontinuities are replaced by transition layers whose thickness is of order ε ^{37,38}. This eliminates mesh dependence, as ε controls the scale of the phase mixture. Accordingly, a large number of hairlike bands are observed issuing

from millimetre size explants⁵, Fig. 1a (where ε would be small compared to explant size), while only a few from single micron scale fibroblasts² (Fig. 1b).

Do the densification patterns in the ECM persist after cell-exerted contractile forces cease^{7,9}? Our active particles (Fig. 5a) contracted upon heating to 39°C, causing densified tethers and radial hairs to appear (Fig. 5b), then expanded to their original radius upon cooling back to 26°C (Fig. 5c) thus providing a controllable method of performing one—or several—loading/unloading cycles. When contraction was reversed, some residual tethers remained (Fig. 5c), but they were thinner and less prominent than ones appearing during particle contraction (Fig. 5b). Many radial bands issuing from particles largely disappeared.

We performed simulations (Fig. 5d-5f) of an active particle pair undergoing quasistatic, gradual contraction, followed by gradual expansion to original size, using the bistable energy density (we matched initial particle diameters, distance and particle contractile strains). Experimental observations confirmed included: (i) a residual weaker, thinner, disjointed tether (Fig. 5f), (ii) most radial bands disappearing, (iii) a new circumferential layer of densification appearing upon re-expansion on each particle boundary (Fig. 5f).

Is inelasticity of collagen fibers necessary for tether/densification pattern formation^{7,9}? To answer this we also performed cycle simulations using the monostable energy. Typical tethers and radial hairs appeared during particle contraction, but disappeared upon re-expansion to original size. This shows that the appearance of localised densification bands is due to the microbuckling instability, which is accounted for in the monostable energy density. Thus under suitable contrac-

tile forces, the densification patterns can exist in an elastic fiber network with fibers that buckle. Whether these patterns persist once contractile forces are removed, depends on whether the densified phase is stable under zero stress. This is the case for the bistable energy density with its equally stable minima, but not for the monostable energy density. Analogously, some austenite-martensite transitions occur under stress only, with martensite disappearing upon its removal; this behaviour is called pseudoelasticity^{26,39}, and is described by monostable-type models. Under different circumstances, such as temperature, residual deformations with phase mixtures persist after loads are removed^{39,42,45}; this behaviour is captured by a bistable energy.

Our model captures complex experiments of Shi et al⁸, where a cut is made between two acini in order to interfere with tether formation. The original tether disappears; instead tethers form that bypass the crack by going around its corners (Fig. 5h, 5g).

How is tether formation involved in aiding and abetting intercellular communication? After acini contract causing a tether to form, individual cells from each acinus start migrating along the tether, towards the acinus at the other end^{4,5,7,8}. Isolated fibroblasts grow appendages toward each other along the tether that forms (Fig. 1b) as a result of their contraction². Given this observed tendency of cells to approach each other, the advantage offered by the biphasic behaviour of the fibrous ECM becomes clear: to detect its neighbours, all a cell has to do is contract, uniformly in all directions, without any cues as to the direction of neighbours. The automatic response of the ECM is to form sharply defined, densified paths (tethers) leading directly to nearby cells. Our model identifies this as a special feature of the instability-driven multiphase behaviour of the ECM,

not possible in stable, single-phase elastic materials.

Taken together, our experiments, model and simulations show that the densification patterns caused by contractile cells in fibrous ECM exhibit many salient features of stress-induced phase transformations in solids, captured by nonlinear models featuring a nonconvex, multi-well strain energy density function^{29–33,38,40–45}. Remarkably, similar nonconvex energies arise naturally in modelling the mechanics of fibrous biomaterials, once the microbuckling instability mechanism is accounted for. Our model is minimal, with a handful of parameters, and intended to demonstrate the necessity of a paradigm shift: Material instability has to be taken seriously if we are to understand the behaviour of fibrous networks. This is what enables the model to capture the distinctive morphology of cell-induced, multiphase, pattern-forming deformations in fibrous ECM for the first time. We expect it will provide new insights into the role played by these singular deformations in cell migration, communication and possibly the alteration of mechanical ECM properties caused by cell-induced densification.

Methods

Experiments with Active Particles

Sample preparation. PNIPAAm particles were created from a water/oil mixture as previously described²¹. In our experiments we used two different sizes of PNIPAAm particles that resulted from two different recipes (described in Supplemental Information). The PNIPAAm particles were embedded in networks of rat tail collagen I (Corning), which was fluorescently labeled with Alexa

Fluor 488 (Thermo Fisher Scientific)²¹. The pH of the collagen was neutralised using 100 mM HEPES buffer to a final concentration of 3 mg/ml. The collagen then polymerised at 27°C for 1 hour. These polymerisation conditions gave fibers of length $19.7 \pm 2 \mu\text{m}$ (mean standard deviation), measured using a previously described method²⁸.

Microscopy and Imaging. Images of PNIPAAm particles embedded in collagen networks were collected using a spinning disk confocal microscope (Yokogawa CSU-X1) with a Nikon Ti-E base and a 20×0.75 NA air objective (Nikon) using a Zyla sCMOS camera (Andor). The particles diameters and the distances between particle centres were measured manually using ImageJ.

Numerical Method

We employ the finite element method, based on a triangulation of the domain Ω . Our approximations for the deformation are sought in the space of continuous piecewise polynomial functions of degree two. Consequently, our computational methods are based on a discrete minimisation problem on the finite element space. In order to capture areas of high densification accurately a local mesh refinement strategy close to the areas of phase transition is adopted.

Challenges include the subtle non-linear character of the problem, and the nearly singular behaviour of solutions in areas where phase transition takes place. It is known that numerical algorithms can become quite subtle exactly at these areas, and thus special care should be given to the reliable resolution of the interfaces.

Incorporating higher gradients into the energy functional, $\varepsilon > 0$ in (3), introduces additional

challenges, because the finite element spaces based on piecewise continuous polynomials have reduced smoothness and are not consistent with the standard energy setting of the model. Furthermore, it is very desirable to have a computational model that works seamlessly when introducing regularisation by higher gradients. We thus use the same discrete spaces in all models considered in our study ($\varepsilon = 0$ and $\varepsilon > 0$). To this end, we adapt to our problem an approach based on the discontinuous Galerkin methodology. Our approximations are still sought on the same spaces of piecewise continuous polynomial functions over a triangulation of the domain, however the energy functional is modified to account for possible discontinuities of normal derivatives at the element faces. We introduce a novel discrete energy functional, which includes terms accounting for the jumps of the higher gradients at the cell interfaces, as well as penalty terms which enforce weak continuity of the higher gradients and coercivity. To be more specific, let \mathbf{y}_h denote a function of the discrete finite element space of piecewise polynomials (C^0 -conforming), then the discretized functional for has the form:

$$\begin{aligned} \Psi_h[\mathbf{y}_h] = & \int_{\Omega} [W(\nabla \mathbf{y}_h) + \varepsilon^2 \left(\frac{1}{2} \sum_{K \in T_h} \int_K |\nabla \nabla \mathbf{y}_h|^2 d \right. \\ & \left. - \sum_{e \in E_h} \left[\int_e \{\{ \nabla \nabla \mathbf{y}_h \} \} \cdot \llbracket \nabla \mathbf{y}_h \otimes \mathbf{n}_e \rrbracket + \frac{60}{h_e} \int_e |\llbracket \nabla \mathbf{y}_h \rrbracket|^2 \right] \right) \end{aligned} \quad (6)$$

where E_h is the set of the interior facets of the triangulation, h_e is the length of the edge e and the average, jump operators $\{\{ \cdot \} \}$, $\llbracket \cdot \rrbracket$ are defined as follows

$$\begin{aligned} \{\{ \nabla \nabla \mathbf{y}_h \} \} &= \frac{1}{2} (\nabla \nabla \mathbf{y}_h^+ + \nabla \nabla \mathbf{y}_h^-) \\ \llbracket \nabla \mathbf{y}_h \otimes \mathbf{n}_e \rrbracket &= \nabla \mathbf{y}_h^+ \otimes \mathbf{n}_e^+ + \nabla \mathbf{y}_h^- \otimes \mathbf{n}_e^- \\ \llbracket \nabla \mathbf{y}_h \rrbracket &= \nabla \mathbf{y}_h^+ - \nabla \mathbf{y}_h^-, \end{aligned}$$

here the superscripts $+$ and $-$ indicate functions evaluation on opposite sides of an edge e , \mathbf{n}_e^+ , \mathbf{n}_e^-

are the corresponding outward normal to the edge and \otimes denotes the tensor product.

The discretization has been implemented in FEniCs⁴⁶. For the minimization of the discrete energy functional a parallelized nonlinear conjugate gradient method⁴⁷ has been developed. The reliability of the computational experiments is guaranteed by a separate detailed mathematical study⁴⁸, which demonstrates the convergence of the discrete numerical solution to the solutions predicted by the model.

The energy functional is minimised using a parallelized version of the nonlinear conjugate gradient method⁴⁷, a successful iterative method for large scale nonlinear optimisation problems. When ellipticity of the corresponding Euler-Lagrange equation for the unregularized problem holds, Newtons method is an efficient nonlinear minimisation technique. However, because ellipticity fails in our model (and phase transition occurs) the Hessian matrix of second derivatives of the energy is not positive definite, thus the nonlinear conjugate gradient is preferred, for both the unregularized and regularised energy functionals.

The reliability of the computational experiments is guaranteed by a separate detailed mathematical study⁴⁸, which demonstrates the convergence of the discrete numerical solution to the solutions predicted by the model. The discretization has been implemented in FEniCs⁴⁶. For the minimization of the discrete energy functional a parallelized nonlinear conjugate gradient method⁴⁷ has been developed, using a popular iterative approach for large scale nonlinear optimisation problems. When ellipticity of the corresponding Euler-Lagrange equation for the unregularized problem holds, Newtons method is an efficient nonlinear minimisation technique. However, because

ellipticity fails in our model (and phase transition occurs) the Hessian matrix of second derivatives of the energy is not positive definite, thus the nonlinear conjugate gradient is preferred, for both the unregularized and regularised energy functionals.

Model

Energy Density. For a single fiber, we introduce the effective stretch λ , which equals the distance between its endpoints divided by its undeformed, or relaxed, length. The energy of a single fiber can be written as $w(\lambda)$ as a function of effective stretch λ . When the fiber is in tension, it is straight and λ equals the actual stretch (strain + 1), while $w(\lambda)$ equals the elastic energy due to stretching of the fiber. When it is in compression, it may be buckled, in which case the elastic bending energy of the fiber can still be expressed as a function $w(\lambda)$ of the distance between its endpoints, hence of the effective stretch λ . See Supplemental Fig. S1a. In order to model a 1D two well energy $w(\lambda)$ for a single fiber like the red curve in Fig. 1d, we start with the derivative $S(\lambda) = dw(\lambda)/d\lambda$, which represents force as a function of stretch. We choose a polynomial that vanishes at 0, 1 and an intermediate value,

$$S(\lambda) = \lambda^5 - (a_m + 1)\lambda^3 + a_m\lambda,$$

to qualitatively represent the curve in Fig. 2e. Here a_m is a parameter that controls the relative height of the two wells (minima) of $w(\lambda)$. Integrating this with respect to λ gives an energy

$$w(\lambda) = \lambda^6/6 - (a_m + 1)\lambda^4/4 + a_m\lambda^2/2 + 1/12 - a_m/4 \quad (7)$$

We model the ECM as a 2D nonlinear elastic continuum undergoing possibly large deformations $\mathbf{y}(\mathbf{x})$ where a particle with reference position vector \mathbf{x} in the undeformed state is mapped to de-

formed position $\mathbf{y} = \mathbf{y}(\mathbf{x})$. The elastic strain energy density of the material can be written as a function $W(\mathbf{F})$ of the deformation gradient $\mathbf{F} = \nabla \mathbf{y}$, which is a 2×2 matrix. We model the random fiber network as an isotropic material, which means that W depends on \mathbf{F} only through the principal stretches λ_1, λ_2 , whose squares are the eigenvalues of the Cauchy-Green deformation matrix $\mathbf{F}^T \mathbf{F}$. Equivalently W is a function of the two deformation invariants $I_1(\mathbf{F}) = \text{tr}(\mathbf{F}^T \mathbf{F}) = \lambda_1^2 + \lambda_2^2$ and $J(\mathbf{F}) = \det \mathbf{F} = \lambda_1 \lambda_2$. Here J is the Jacobian determinant of the deformation and the ratio of deformed density ρ to reference density ρ_0 satisfies $\rho/\rho_0 = 1/J$.

To connect the single fiber energy with the 2D strain energy density W we follow ^{24,25}. We assume the network contains a uniform distribution of fibers. A homogeneous deformation (with constant strain) is equivalent to a biaxial stretch in two orthogonal directions with stretches λ_1, λ_2 . A fiber of undeformed length l that makes an angle θ with the principal stretch axes in the undeformed state, will have endpoints at $(0, 0)$ and $(l \cos \theta, l \sin \theta)$. After deformation the latter will become $(\lambda_1 l \cos \theta, \lambda_2 l \sin \theta)$. As a result, the stretch ratio of the fiber will be $\lambda(\theta) = \sqrt{(\lambda_1 \cos \theta)^2 + (\lambda_2 \sin \theta)^2}$, and its energy will be $w(\lambda(\theta))$. Summing over all fiber orientation angles θ , we find the elastic energy density of the network

$$\hat{W}(\lambda_1, \lambda_2) = \frac{1}{2\pi} \int_0^{2\pi} w(\lambda(\theta)) d\theta = \frac{1}{2\pi} \int_0^{2\pi} w \left(\sqrt{(\lambda_1 \cos \theta)^2 + (\lambda_2 \sin \theta)^2} \right) d\theta,$$

which gives (1). It turns out that for $w(\lambda)$ given by (7), the integral in (1) can be evaluated explicitly:

$$\tilde{W}(\mathbf{F}) = \frac{1}{96} [5I_1^3 - 12I_1 J^2 - (1 + a_m)(9I_1^2 - 12J^2) + 24a_m I_1 + 8]. \quad (8)$$

Here $I_1 = \text{tr} \mathbf{F}^T \mathbf{F} = \lambda_1^2 + \lambda_2^2$ and $J = \det \mathbf{F} = \lambda_1 \lambda_2$ are the 2D deformation invariants. We then add a fiber volume penalty term to the energy to account for resistance of densified fibers

to complete crushing by virtue of their nonzero volume. This term increases the energy abruptly when the Jacobian (volume ratio) $J = \det \mathbf{F}$ becomes less than a small positive constant $b \ll 1$, while it becomes negligible as J increases from b . Such a function is given by

$$\Phi(J) = \exp[A(b - J)] \quad (9)$$

(Supplemental Fig. S1b) where A is a large positive constant. The total energy is

$$W^*(\mathbf{F}) = \tilde{W}(\mathbf{F}) + \Phi(\det \mathbf{F})$$

Model for Active Particles. We consider two models, one for a cell/acinus and another for active particles. The soft model for cells or acini is given by (4); see also Supplemental Fig. S1c. Stiff active particles are modelled as contracting spheres. Each point on their circumference is connected to the matrix by a linear spring of zero natural length.

$$C\{\mathbf{y}; \mathbf{z}_1, \dots, \mathbf{z}_n\} = \sum_{i=1}^n \int_{\Gamma_i} \frac{k}{2} |\mathbf{y}(\mathbf{x}) - \mathbf{z}_i - (1 - u_0/R)(\mathbf{x} - \bar{\mathbf{z}}_i)|^2 ds_{\mathbf{x}} \quad (10)$$

where Γ_i is the boundary of the i^{th} cavity ($i = 1, \dots, n$), k is the spring stiffness, \mathbf{z}_i the variable (deformed) centre position of the i^{th} cell, $\bar{\mathbf{z}}_i$ is its undeformed position, R the undeformed radius, and u_0 the particle radius contraction. See Supplemental Fig. S1d.

Acknowledgments. The work of PR, CG and GG was partially supported by the EU Horizon 2020 Research and Innovation Programme under the Marie Skłodowska-Curie project ModComp-Shock (modcompshock.eu) agreement No 642768 The work of JN and MP and was partially

supported by National Science Foundation grant number CMMI-1749400. GR acknowledges the support of the National Science Foundation (DMR No. 0520565) through the Center for Science and Engineering of Materials at the California Institute of Technology. We thank Brian Burkel for assistance in microscopy.

Author Contributions. PR, GR and JN planned the research. GG and PR developed the model. GG and CG developed the numerical method. GG performed the simulations. MP and JN designed the experiments. MP performed the experiments; MP and JN analysed the data. All authors discussed and analyzed the results and contributed to writing the manuscript.

1. Rudnicki, M. S. *et al.* Nonlinear strain stiffening is not sufficient to explain how far cells can feel on fibrous protein gels. *Biophysical Journal* **105**, 11–20 (2013). URL <http://dx.doi.org/10.1016/j.bpj.2013.05.032>.
2. Notbohm, J., Lesman, A., Rosakis, P., Tirrell, D. A. & Ravichandran, G. Microbuckling of fibrin provides a mechanism for cell mechanosensing. *Journal of the Royal Society, Interface / the Royal Society* **12**, 20150320 (2015). URL <http://rsif.royalsocietypublishing.org/content/12/108/20150320.abstract>.
3. Weiss, P. In vitro experiments on the factors determining the course of the outgrowing nerve fiber. *Journal of Experimental Zoology* **68**, 393–448 (1934).
4. Harris, A. K., Stopak, D. & Wild, P. Fibroblast traction as a mechanism for collagen morphogenesis. *Nature* **290**, 249–251 (1981).

5. Stopak, D. & Harris, A. K. Connective tissue morphogenesis by fibroblast traction: I. tissue culture observations. *Developmental biology* **90**, 383–398 (1982).
6. Korff, T. & Augustin, H. G. Tensional forces in fibrillar extracellular matrices control directional capillary sprouting. *J Cell Sci* **112**, 3249–3258 (1999).
7. Vader, D., Kabla, A., Weitz, D. & Mahadevan, L. Strain-induced alignment in collagen gels. *PloS one* **4**, e5902 (2009).
8. Shi, Q. *et al.* Rapid disorganization of mechanically interacting systems of mammary acini. *Proceedings of the National Academy of Sciences* **111**, 658–663 (2014).
9. Ban, E. *et al.* Mechanisms of plastic deformation in collagen networks induced by cellular forces. *Biophysical journal* **114**, 450–461 (2018).
10. Yu, H., Mouw, J. K. & Weaver, V. M. Forcing form and function: biomechanical regulation of tumor evolution. *Trends in cell biology* **21**, 47–56 (2011).
11. Winer, J. P., Oake, S. & Janmey, P. A. Non-linear elasticity of extracellular matrices enables contractile cells to communicate local position and orientation. *PloS one* **4**, e6382 (2009).
12. Wang, H., Abhilash, A., Chen, C. S., Wells, R. G. & Shenoy, V. B. Long-range force transmission in fibrous matrices enabled by tension-driven alignment of fibers. *Biophysical journal* **107**, 2592–2603 (2014).
13. Rosakis, P., Notbohm, J. & Ravichandran, G. A model for compression-weakening materials and the elastic fields due to contractile cells. *Journal of the Mechanics and Physics of*

- Solids* **85**, 16–32 (2015). URL <http://linkinghub.elsevier.com/retrieve/pii/S0022509615300958.1412.2612>.
14. Lakes, R., Rosakis, P. & Ruina, a. Microbuckling instability in elastomeric cellular solids. *Journal of Materials Science* **28**, 4667–4672 (1993).
 15. Kim, O. V. *et al.* Foam-like compression behavior of fibrin networks. *Biomechanics and Modeling in Mechanobiology* (2015). URL <http://www.ncbi.nlm.nih.gov/pubmed/25982442> \backslash delimiter"026E30F\$n<http://link.springer.com/10.1007/s10237-015-0683-z> \backslash delimiter"026E30F\$n"<http://dx.doi.org/10.1007/s10237-015-0683-z>.
 16. Van Der Rijt, J. A., Van Der Werf, K. O., Bennink, M. L., Dijkstra, P. J. & Feijen, J. Micromechanical testing of individual collagen fibrils. *Macromolecular bioscience* **6**, 697–702 (2006).
 17. Hudson, N. E. *et al.* Stiffening of individual fibrin fibers equitably distributes strain and strengthens networks. *Biophysical journal* **98**, 1632–1640 (2010).
 18. Piechocka, I. K., Bacabac, R. G., Potters, M., MacKintosh, F. C. & Koenderink, G. H. Structural hierarchy governs fibrin gel mechanics. *Biophysical journal* **98**, 2281–2289 (2010).
 19. Münster, S. *et al.* Strain history dependence of the nonlinear stress response of fibrin and collagen networks. *Proceedings of the National Academy of Sciences* **110**, 12197–12202 (2013).
 20. Kim, O. V., Litvinov, R. I., Weisel, J. W. & Alber, M. S. Structural basis for the nonlinear mechanics of fibrin networks under compression. *Biomaterials* **35**, 6739–6749 (2014).

21. Burkel, B. & Notbohm, J. Mechanical response of collagen networks to nonuniform microscale loads. *Soft matter* **13**, 5749–5758 (2017).
22. Simhadri, J. J. & Chandran, P. L. Capturing 3d large-strain euler-bending filament dynamics in fibrous media simulations; sample case of compression collapse in dendritic actin network. *Scientific reports* **9**, 3990 (2019).
23. Treloar, L. R. G. *The physics of rubber elasticity* (Oxford University Press, USA, 1975).
24. Vainchtein, A., Klein, P., Gao, H. & Huang, Y. A strain-gradient virtual-internal-bond model. *Modeling and Simulation-based Life Cycle Engineering* 31–46 (2002).
25. Gloria, A., Le Tallec, P. & Vidrascu, M. Foundation, analysis, and numerical investigation of a variational network-based model for rubber. *Continuum mechanics and thermodynamics* **26**, 1–31 (2014).
26. Otsuka, K. & Wayman, C. M. *Shape memory materials* (Cambridge university press, 1999).
27. Vos, B. E. *et al.* Programming the mechanics of cohesive fiber networks by compression. *Soft matter* **13**, 8886–8893 (2017).
28. Burkel, B., Proestaki, M., Tyznik, S. & Notbohm, J. Heterogeneity and nonaffinity of cell-induced matrix displacements. *Physical Review E* **98**, 052410 (2018).
29. Knowles, J. K. & Sternberg, E. On the failure of ellipticity and the emergence of discontinuous deformation gradients in plane finite elastostatics. *Journal of Elasticity* **8**, 329–379 (1978). URL <http://dx.doi.org/10.1007/BF00049187>

delimiter"026E30F\$nhhttp://www.springerlink.com/content/
q08517v013340160/\$\delimiter"026E30F\$nhhttp://www.springerlink.
com/content/q08517v013340160/fulltext.pdf.

30. Ball, J. M. & James, R. D. Fine phase mixtures as minimizers of energy. *Archive for Rational Mechanics and Analysis* **100**, 13–52 (1987).
31. Ball, J. & Carstensen, C. Compatibility conditions for microstructures and the austenite–martensite transition. *Materials Science and Engineering: A* **273**, 231–236 (1999).
32. Abeyaratne, R. & Knowles, J. K. *Evolution of phase transitions: a continuum theory* (Cambridge University Press, 2006).
33. Ball, J. M. Convexity conditions and existence theorems in nonlinear elasticity. *Archive for rational mechanics and Analysis* **63**, 337–403 (1976).
34. Knowles, J. K. & Sternberg, E. On the failure of ellipticity of the equations for finite elastostatic plane strain. *Archive for Rational Mechanics and Analysis* **63**, 321–336 (1976).
35. Rosakis, P. Ellipticity and deformations with discontinuous gradients in finite elastostatics. *Archive for Rational Mechanics and Analysis* **109**, 1–37 (1990).
36. Bardenhagen, S. & Triantafyllidis, N. Derivation of higher order gradient continuum theories in 2, 3-d non-linear elasticity from periodic lattice models. *Journal of the Mechanics and Physics of Solids* **42**, 111–139 (1994).

37. Triantafyllidis, N. & Aifantis, E. C. A gradient approach to localization of deformation. i. hyperelastic materials. *Journal of Elasticity* **16**, 225–237 (1986).
38. Ball, J. & Crooks, E. Local minimizers and planar interfaces in a phase-transition model with interfacial energy. *Calculus of Variations and Partial Differential Equations* **40**, 501–538 (2011).
39. Delaey, L., Krishnan, R., Tas, H. & Warlimont, H. Thermoelasticity, pseudoelasticity and the memory effects associated with martensitic transformations. *Journal of Materials Science* **9**, 1521–1535 (1974).
40. James, R. D., Kohn, R. V. & Shield, T. Modeling of branched needle microstructures at the edge of a martensite laminate. *Le Journal de Physique IV* **5**, C8–253 (1995).
41. Dacorogna, B. *Direct methods in the calculus of variations*, vol. 78 (Springer Science & Business Media, 2007).
42. Bhattacharya, K. *Microstructure of martensite: why it forms and how it gives rise to the shape-memory effect*, vol. 2 (Oxford University Press, 2003).
43. Luskin, M. On the computation of crystalline microstructure. *Acta numerica* **5**, 191–257 (1996).
44. Healey, T. J. & Miller, U. Two-phase equilibria in the anti-plane shear of an elastic solid with interfacial effects via global bifurcation. *Proceedings of the Royal Society of London A: Mathematical, Physical and Engineering Sciences* **463**, 1117–1134 (2007).

45. Abeyaratne, R., Chu, C. & James, R. D. Kinetics of materials with wiggly energies: theory and application to the evolution of twinning microstructures in a cu-al-ni shape memory alloy. *Philosophical Magazine A* **73**, 457–497 (1996).
46. Alnæs, M. S. *et al.* The fenics project version 1.5. *Archive of Numerical Software* **3** (2015).
47. Nocedal, J. & Wright, S. J. *Numerical optimization*. Springer Series in Operations Research and Financial Engineering (Springer, Berlin, 2006). URL <http://opac.inria.fr/record=b1120179>. NEOS guide <http://www-fp.mcs.anl.gov/otc/Guide/>.
48. Grekas, G. *Modelling, Analysis and Computation of Cell-Induced Phase Transitions in Fibrous Biomaterials*. Ph.D. thesis, University of Crete (2019).

Supplemental Information

Compressive Stretch Estimate. To estimate compressive strains we note that in the tether the density ratio ρ/ρ_0 of deformed to undeformed density is typically in the range⁹ 3-5 also observed in our experiments. From mass balance we have that $\rho\lambda_1\lambda_2 = \rho_0$. Thus the inequality $\rho/\rho_0 \geq 3$ and the fact that the tether is in longitudinal tension so that $\lambda_2 \geq 1$ give the inequality $\lambda_1 < 1/3$. This is roughly 70% compressive strain $\varepsilon_1 = \lambda_1 - 1 \approx -0.67$.

Stiffness Loss. For a network of fibers with force-stretch relation as in Fig. 2a, we show that the orientation averaged stress goes to zero in the crushing limit. Consider uniaxial compression along the y -axis with stretch $0 < \lambda_c < 1$ and tension along the x -axis with stretch $\lambda_t \geq 1$. Then a fiber that makes an angle θ with the compression (y)-axis in the undeformed state, will make an angle

θ_* such that $\tan \theta_* = (\lambda_t/\lambda_c) \tan \theta$. Since $\lambda_t/\lambda_c > 1$ we have $\theta_* > \theta$ and the angle of the fiber with the direction of compression increases and approaches 90° in the crushing limit as $\lambda_c \rightarrow 0$. This reorientation tends to decrease the component of the load in the compression direction a fiber can sustain. For example, consider uniaxial compressive stretch with $\lambda_t \geq 1$ fixed and $\lambda_c \rightarrow 0$. The fiber stretch is $\sqrt{(\lambda_c \cos \theta)^2 + (\lambda_t \sin \theta)^2}$. The component of fiber axial force in the y direction of compression is $T = S \cos \theta_*$. Now S is bounded in compression and as $\lambda_c \rightarrow 0$, $\theta_* \rightarrow \pi/2$ so $\cos \theta_* \rightarrow 0$. As a result the component of the fiber force along the compression direction $T \rightarrow 0$. The compressive stress is $\int T d\theta = \int S \cos \theta_* d\theta$. Now $S \cos \theta_*$ is bounded for compression and $\cos \theta_*$ converges (almost everywhere) to zero (except when $\theta = 0$) so bounded convergence implies that $\int T d\theta \rightarrow 0$ as $\lambda_c \rightarrow 0$. As a result the material fails to sustain uniaxial compressive stress in the crushing limit, and the qualitative behaviour is necessarily as in Fig. 2b.

Single Fiber Behaviour. Modelling the force-stretch relation of a single fiber depends on the post-buckling behaviour of a flexible beam, which can be quite complicated as buckling is a bifurcation/instability phenomenon. There are typically three main types of post-buckling response $S(\lambda)$, depending on whether stability is maintained or lost on the bifurcating branch of buckled states²², and whether it is later regained if lost: (i) Stable post-buckling, where stiffness is diminished but load carrying capacity in compression is not lost (as λ decreases below 1). An example is $S(\lambda) = k(\lambda^3 - 1)$ with $k > 0$ a constant (Fig. 2a). (ii) Unstable (collapse) post-buckling, where the stiffness becomes negative (stability is lost) with increasing compression, e.g., $S(\lambda) = k(\lambda^5 - \lambda)$. (of the form shown in Fig. 2b). (iii) Snap-through post-buckling, where stability is first lost but eventually regained at higher compression²², for example $S(\lambda) = k(\lambda^5 - 3\lambda^3/2 + \lambda/2)$ (qualita-

tively as in Fig. 2e).

Ellipticity Loss. The strong ellipticity condition³⁴ plays a central role in coherent phase transformations in solids. It is closely related to the rank-one convexity condition³³ and implies local stability of the material. In one dimension it is equivalent to positive slope (tangent modulus) of the (nonlinear) stress-strain curve, so it would fail for some intermediate strains where the slope is negative in Fig. 2c, 2f. In higher dimensions its meaning is more complex³⁵. An elastic energy density function that is globally strongly elliptic cannot sustain strain discontinuities and phase transitions²⁹. In order to determine for what values of the principal stretches strong ellipticity fails in our model energy density functions W and W^* , we use the criteria of Knowles & Sternberg³⁴. The result is shown in Supplemental Fig. S2d, S2e.

Compatibility. The compatibility condition for strain discontinuities states that for two different values of the deformation gradient \mathbf{F}_1 and \mathbf{F}_2 to occur on either side of a strain discontinuity surface, across which the displacement is continuous (such as a coherent phase boundary or twin boundary), they must be rank-one connected, namely satisfy $\mathbf{F}_2 - \mathbf{F}_1 = \mathbf{a} \otimes \mathbf{n}$ for some vector \mathbf{a} , where \mathbf{n} is the unit normal to the surface²⁹. In case $\mathbf{F}_1 = \mathbf{1}$ (undeformed state) then the principal stretches of \mathbf{F}_2 must then satisfy the inequalities^{30,31}

$$\lambda_2 \geq 1, \quad \lambda_1 \leq 1 \quad (s1)$$

It turns out that in our model the minimal energy principal stretches $(\lambda_1^*, \lambda_2^*)$ at the energy well corresponding to the densified phase always satisfy these inequalities. In the specific example of the bistable energy W^* used in our simulations, $(\lambda_1^*, \lambda_2^*) = (0.2, 1.06)$ (Fig. S2a). Since the energy

is a symmetric function of (λ_1, λ_2) , the minimum at $(\lambda_2^*, \lambda_1^*)$ corresponds to the same state as its $(\lambda_1^*, \lambda_2^*)$. The additional minimum at $(\lambda_1, \lambda_2) = (0.45, 0.45)$ is not compatible with the undeformed state $(1, 1)$ since it violates Eq. (s1). The principal stretches in our simulations are never observed to take values at or near this state, This further illustrates the role of compatibility.

In Supplemental Fig. S3 the phase boundary between the tether and the rest of the ECM is roughly parallel to a principal direction of stretch. In that case compatibility requires that the stretch in the direction parallel to the phase boundary has to be continuous across it (in this case the tensile stretch λ_{max}) whereas the compressive one λ_{min} may be discontinuous as seen in the simulation

Principal Stretches. An isotropic elastic energy density function $W(\mathbf{F})$ in 2D, normally expressed in terms of the deformation gradient matrix \mathbf{F} , can be written as a function of the principal stretches $\lambda_2 \geq \lambda_1 > 0$ which are the eigenvalues of the right stretch tensor $\mathbf{U} = (\mathbf{F}^T \mathbf{F})^{1/2}$. Typically in a tether between similar cells, there is moderate tension along its axis and sever compression normal to it, thus the principal axes of stretch roughly correspond to these two directions. Because of compatibility, the compressive stretch λ_1 can jump across the tether boundary, but the tensile one cannot, as it stretches the material roughly parallel to the boundary. This is encountered in experiments⁹ and captured in our simulations as seen in Supplemental Fig. S3

Experiments: Generation of PNIPAAm Particles. PNIPAAm particles were generated using two different recipes, one giving larger particles (diameter 150 μm) and the other giving smaller particles (diameter 75 μm). To generate the larger particles, kerosene with 3.5% Span 80 (Tokyo

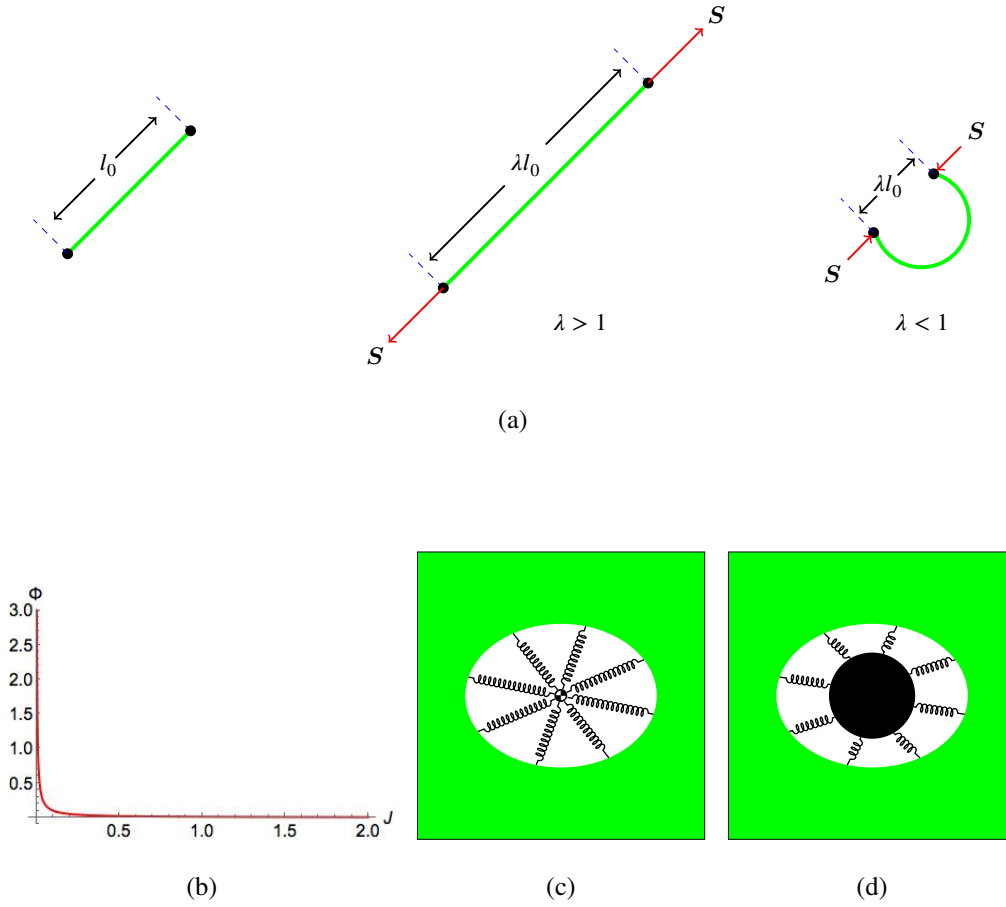


Figure S1: Various aspects of the Model. (a) The effective stretch λ of a single fiber is the ratio of deformed to undeformed distance l_0 of its endpoints. From left to right: relaxed (undeformed), under tension, buckled under compression. Red arrows represent forces. (b) Fiber volume penalty function $\Phi(J)$. (c) Soft model for cell or acini, contributing term (4) to the total energy. (d) Stiff model for active PNIPAAm particles contributing term (10) to the total energy.

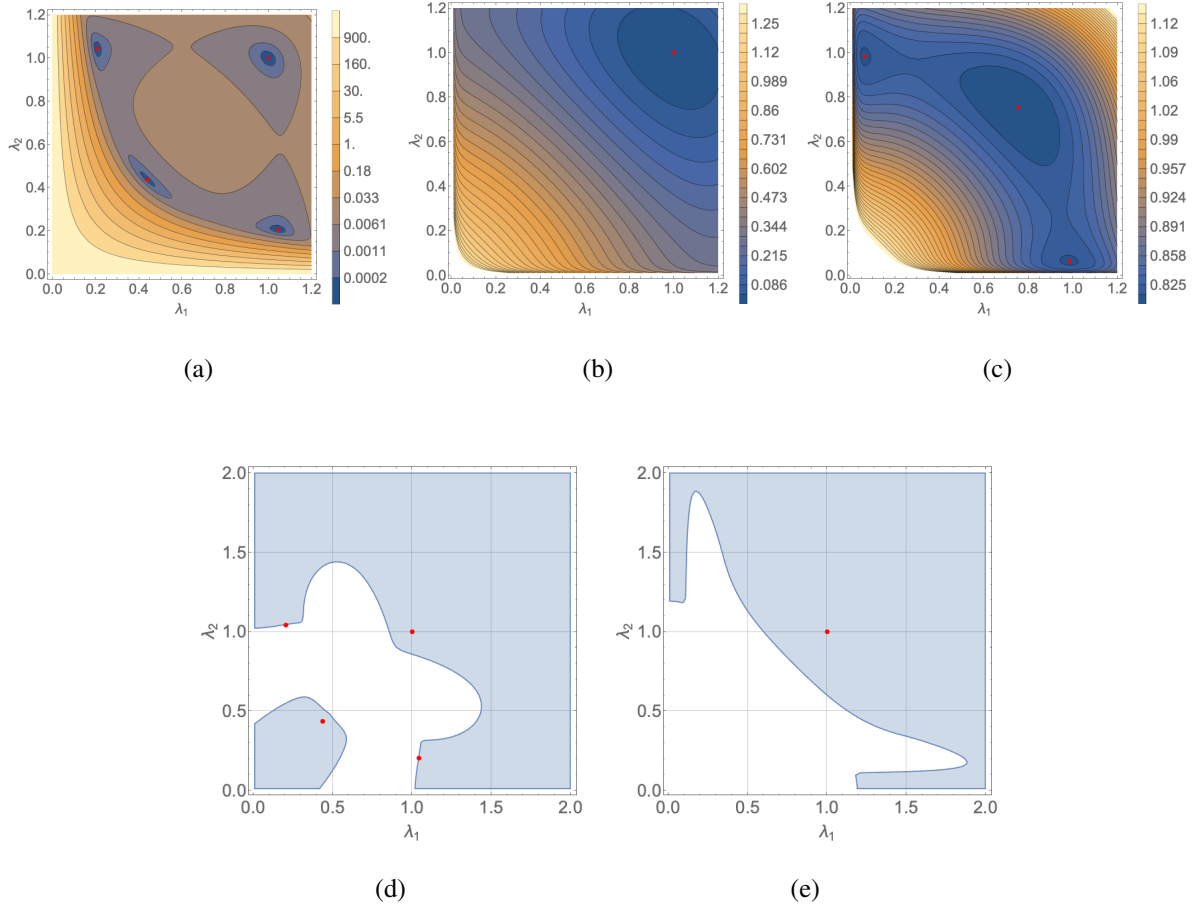


Figure S2: (a)-(c) Level curves (black) and local minima (red dots) of various energy density functions in the (λ_1, λ_2) -plane. (a) The bistable energy W^* . (b) The monostable energy W . (c) The Gibbs free energy $W(\mathbf{F}) - \mathbf{S} \cdot \mathbf{F}$ for a suitable compressive stress \mathbf{S} . Pairs of minima of the form (λ_1, λ_2) and (λ_2, λ_1) correspond to the same state. (d)-(e) Domains of validity (light blue) and failure of the strong ellipticity condition (white): (d) of the bistable energy W^* and (e) of the monostable energy W .

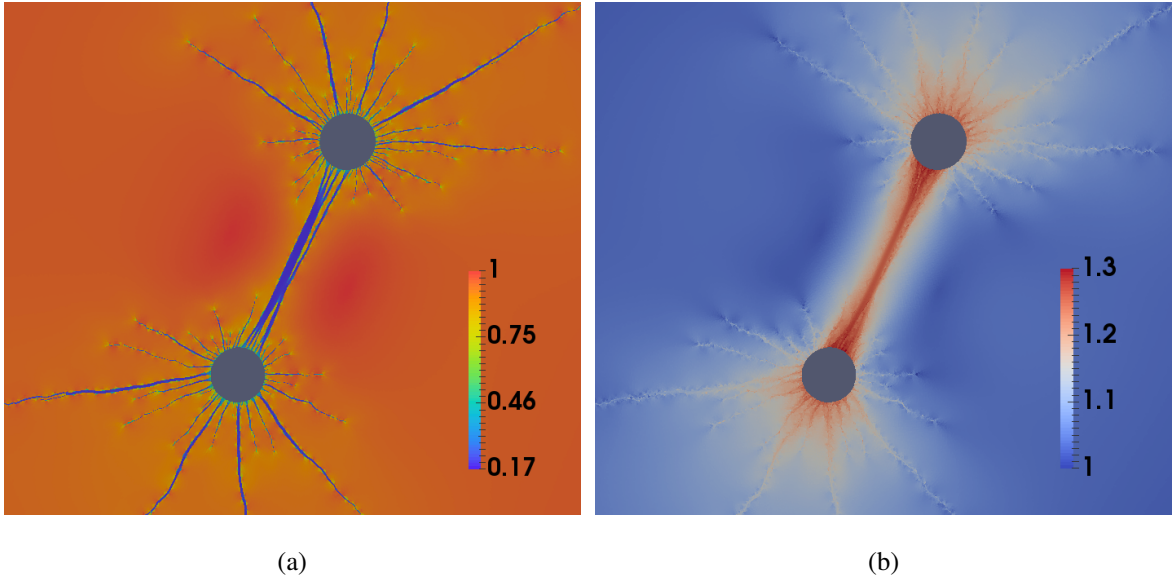


Figure S3: The principal stretches (a) $\lambda_{min} < 1$ in and (b) $\lambda_{max} > 1$ from the simulation shown in Fig. 5e. Note sharp change in λ_{min} across the tether boundary indicating a discontinuity, and gradual change in λ_{max} as predicted by compatibility.

Chemical Industries) was degassed under vacuum for 1 hour. It was then maintained under nitrogen for 10 minutes before stirring at 350 rpm at 22°C. A solution containing 1 g N-isopolyacrylamide (Sigma), 0.15 g bis-acrylamide (Bio-Rad), 0.05 g Ammonium Persulfate (Bio-Rad) and 1.5 ml of 1 × tris-buffered saline was prepared. 10 µl TEMED (Bio-Rad) was added, and the solution was immediately added to the kerosene. To generate the smaller particles, cyclohexane, rather than kerosene, with 3.5% Span 80 was used as the solvent, and stirring occurred at 450 rpm instead of 350 rpm. A solution of 1 g N-isopolyacrylamide (Sigma), 0.075 g bis-acrylamide (Bio-Rad), 0.05 g Ammonium Persulfate (Bio-Rad), 1.5 ml of 1 × tris-buffered saline and 3.75 ml deionised water was prepared. Again, 10 µl TEMED (Bio-Rad) was added, and the solution was immediately combined with the cyclohexane. For both large and small particles, the solutions were stirred for 30 min, and then the PNIPAAm particles were allowed to settle overnight. The particles were then washed with hexane and again allowed to settle. Washes were repeated with isopropyl alcohol, ethanol, and finally deionised water. The particles were then filtered with a cell strainer to keep particles of diameter > 40 µm. The particles were resuspended in 1 × PBS.

Experiments: Temperature control while imaging. The temperature was controlled with an H301 incubator (Okolab) mounted on the microscope stage and controlled with an UNO controller (Okolab). To verify that the samples reached the desired temperature, we used a digital thermometer having accuracy of 0.1°C (Fisherbrand Traceable) with its probe inside a dish with water placed next to the samples. Images were collected when samples were at 26°C (reference state) and 39°C (contracted state).